JGR Space Physics

RESEARCH ARTICLE

10.1029/2021JA029229

Key Points:

- A high-frequency beacon network in Peru used for inferring ionospheric electron number densities regionally has been greatly expanded
- Sensitivity analysis and absorption computation turn signal power into additional, useful observable
- Regional electron density data can be combined with incoherent scatter radar measurements for studying and forecasting space weather

Correspondence to:

D. L. Hysell,
david.hysell@cornell.edu

Citation:

Hysell, D. L., Rojas, E., Goldberg, H., Milla, M. A., Kuyeng, K., Valdez, A., et al. (2021). Mapping irregularities in the postsunset equatorial ionosphere with an expanded network of HF beacons. *Journal of Geophysical Research: Space Physics*, *126*, e2021JA029229. https://doi.org/10.1029/2021JA029229

Received 8 FEB 2021
Accepted 1 JUL 2021

Mapping Irregularities in the Postsunset Equatorial Ionosphere With an Expanded Network of HF Beacons

D. L. Hysell[1], E. Rojas[1], H. Goldberg[1], M. A. Milla[2], K. Kuyeng[2], A. Valdez[2], Y. T. Morton[3], and H. Bourne[3]

[1]Earth and Atmospheric Sciences, Cornell University, Ithaca, NY, USA, [2]Radio Observatorio de Jicamarca, Instituto Geofísico del Peru, Lima, Peru, [3]Department of Aerospace Engineering Sciences, University of Colorado, Boulder, CO, USA

Abstract Data from a network of high-frequency (HF) beacons deployed in Peru are used to estimate the regional ionospheric electron density in a volume. Pseudorange, accumulated carrier phase, and signal power measurements for each of the 36 ray paths provided by the network at a 1 min cadence are incorporated in the estimates. Additional data from the Jicamarca incoherent scatter radar, the Jicamarca sounder, and GPS receivers can also be incorporated. The electron density model is estimated as the solution to a global optimization problem that uses ray tracing in the forward model. The electron density is parametrized in terms of B-splines in the horizontal direction and generalized Chapman functions or related functions in the vertical. Variational sensitivity analysis has been added to the method to allow for the utilization of the signal power observable which gives additional information about the morphology of the bottomside F region as well as absorption including absorption in the D and E regions. The goal of the effort is to provide contextual information for improving numerical forecasts of plasma interchange instabilities in the postsunset F region ionosphere associated with equatorial spread F (ESF). Data from two ESF campaigns are presented. In one experiment, the HF data revealed the presence of a large-scale bottomside deformation that seems to have led to instability under otherwise inauspicious conditions. In another experiment, gradual variations in HF signal power were found to be related to the varying shape of the bottomside F layer.

1. Background and Motivation

One of the most common manifestations of space weather is the spontaneous generation of broadband plasma density irregularities in the postsunset equatorial F-region ionosphere. The phenomenon, often referred to as equatorial spread F (ESF) because of the spreading it produces in ionogram traces (Booker & Wells, 1938), is attributed to interchange instability in the F region which can become unstably stratified with the cessation of photoionization. The connection between ESF and interchange instabilities was established by Woodman and La Hoz (1976) who were the first to render coherent backscatter radar profiles observed at the Jicamarca Radio Observatory in range-time-intensity (RTI) image format. Their images resembled numerical simulations of interchange instabilities in barium clouds (e.g., Ossakow, 1981). Earlier, working also at Jicamarca, Farley et al (1970) had established a causal relationship between the height of the F layer at sunset and the occurrence probability of ESF, a finding which is consistent with if not uniquely indicative of interchange instability. Later, true images of large-scale irregularities associated with ESF were observed with the ALTAIR radar on Kwajalein which can scan from horizon to horizon (Tsunoda et al., 1979). These, together with increasingly accurate and finely resolved numerical simulations, cemented the link between ESF and ionospheric interchange instability (see e.g., Aveiro et al., 2011; Keskinen & Vadas, 2009; Keskinen et al., 1980; Krall et al., 2009; Zalesak et al., 1982, 1990; Yokoyama et al., 2014; Zargham & Seyler, 1989).

Forecasting ESF has become imperative because of the hazard it poses to vital radio communication, navigation, and imaging systems which can be degraded by the deep plasma density irregularities ESF produces. However, reliable forecasts of ESF, which exhibits considerable day-to-day variability, have been elusive. Assuming that the physics of plasma interchange instabilities is sufficiently well understood, there are three possible explanations. First, the system could be chaotic. This seems unlikely; in the collisional regime where most ESF takes place, the system is not turbulent, and the most important nonlinearity in the governing equations is associated mainly with plasma steepening (Zargham & Seyler, 1987, 1989). Second, the most important drivers, the background electric fields and winds, may be inadequately specified. This possibility was addressed in a series of studies at Jicamarca (see Hysell et al., 2015 and references therein). In these studies, the occurrence and non-occurrence of irregularities in the postsunset sector was reproduced in most cases in simulations using drivers inferred from Jicamarca incoherent scatter measurements. The "forecasts" were not entirely accurate, however, as the simulations failed to predict the occurrence of irregularities in a few instances.

This finding points to a third explanation which is inadequately specified initial conditions. Results from a recent sounding rocket campaign from Kwajalein point to the existence of subtle, large-scale fluctuations in the bottomside F region at sunset which can influence the morphology of the irregularities that form later (Hysell et al., 2020). The fluctuations, which were identified previously by Tsunoda et al. (2010), seem to be too large in scale to be produced purely by plasma processes and may be indicative of neutral waves in the thermosphere or lower thermosphere, a subject which has received considerable attention in the literature (e.g., Abdu et al., 2009; Huang et al., 1994; Kelley et al., 1981; Keskinen & Vadas, 2009; Krall et al., 2013; Röttger, 1981; Singh et al., 1997; Taori et al., 2011; Tsunoda, 2010).

Here, we explore the possibility of establishing the initial conditions for forecast simulations of ESF using information derived from HF beacons. A network of HF beacon transmitters and receivers was established recently around the Jicamarca Radio Observatory to estimate the electron density in an ionospheric volume surrounding the observatory. The beacon stations employ pseudo random noise (PRN) coding which permits pseudorange measurements. Preliminary studies to assess the practicality of collecting HF datasets routinely from remote, distributed locations and inferring the electron density distribution from them regionally were performed Hysell et al. (2016) and Hysell et al. (2018). Since those studies, the number of stations in the network has grown considerably. Furthermore, other observables, including the Doppler shift (or beat carrier phase) and the signal power, are now being considered in the electron density retrievals. The effort has moved beyond the proof-of-concept stage to the point where it will soon be practical to use the beacon data to initialize and/or force ESF forecast direct numerical simulations (DNS).

Below, we discuss the methods used to estimate electron number densities from beacon data. We demonstrate the methods with sample data collected in 2019. The role of the beacon data in an ESF forecast strategy is then described.

2. Methods

Estimating ionospheric parameters from HF radio measurements is an inverse problem rooted in control theory and constrained partial differential equation optimization. We consider the limit of geometric optics where the radio signals are described by rays. The rays are governed by Fermat's principle which demands that the phase integral over a raypath with fixed boundaries be stationary. Here, the boundaries are set by the transmitter and receiver locations. The constraint comes from the dispersion relation obeyed by the wave in the medium it occupies. Finding the rays which satisfy the boundary conditions and reproduce measurements is an optimization problem.

Raytracing can be performed using direct variational methods and numerical relaxation. An example of this approach is given by Coleman (2011). Another approach involves converting the variational problem into a system of coupled first-order differential equations using the principles of analytic mechanics (e.g., Landau & Lifshitz, 1976). The result are Hamilton's equations which describe the evolution of the generalized ray position $\mathbf{x} \in \mathbb{R}^3$ and its conjugate generalized momentum $\mathbf{p} \in \mathbb{R}^3$ in terms of a Hamiltonian $H(\mathbf{x}, \mathbf{p}, \omega, t)$. The momentum and the wave vector $\mathbf{k}$ are related through a metric tensor that depends on the coordinate system in use.

Hamilton's equations are solved using numerical quadrature (ray shooting). Here, as in Hysell et al. (2018), ray shooting is performed in an inner loop to establish the endpoint of the rays. The parametrized ionosphere in between is then modified to minimize the discrepancy between observed and predicted ray parameters. It is generally desirable to compute not only the state parameters x and k along the ray but also their sensitivity to one or more control parameters. This is useful both for determining the endpoints of the rays and for focusing (see below). Sensitivity analysis can be performed at first or second order where the gradient and the Hessian of the state parameters with respect to the control parameters are found, respectively. The problem is simplified if the control parameters are just the ray initial conditions. For a general review of sensitivity analysis, see Cacuci et al. (1980).

A number of approaches to sensitivity analysis have been developed. One is the brute-force method in which perturbations are introduced in the initial conditions for ray shooting and finite differences are applied to the results. The advantage of this approach is coding simplicity. The main disadvantage is accuracy; large perturbations are subject to quantization error, and small perturbations to roundoff error. A second approach is the direct variational method in which the differential equations describing the control-vector sensitivities are derived and integrated alongside the original raytracing equations (Nickisch, 1988; Sambridge & Kennett, 1990; Västberg & Lundborg, 1996). The computational cost of the method is related to the number of control parameters which should therefore not be very large. (A variant of the approach involves solving the sensitivity equations using the method of Green's functions which may be more numerically efficient in cases where the number of control parameters is large (Hwang et al., 1978)).

Another approach is the adjoint method which is a key tool in data assimilation and machine learning (Cao et al., 2003; Tromp et al., 2005). The computational cost of the adjoint method is related to the number of constraints rather than the number of control parameters. Consider a Lagrangian function that combines an objective function (which measures mismatches in the boundary conditions for the ray) with the constraint equation (Hamilton's equations, each multiplied by a Lagrange multiplier). Differentiating the Lagrangian with respect to the control variables yields, after some manipulation, two new equations. One is the desired sensitivity equation, and the other is the adjoint equation. The adjoint equation will be formally similar to the original constraint equation except with the Lagrange multipliers replacing the original state variables. Crucially, it may be no harder to integrate (along ray paths) than the original constraint equation. The analysis proceeds as follows: (a) Integration of the original constraint equations takes place in the forward direction as usual. (b) Integration of the adjoint equation takes place in the backward direction. (c) The results are used to calculate the sensitivities with one final path integration. Note that the adjoint problem can be applied not just to fixing ray endpoints and focusing but to the larger problem of adjusting ionospheric model parameters for optimal congruence with the experimental observables (e.g., M. Psiaki, 2019).

A final means of sensitivity analysis is automatic differentiation (e.g., Bartholomew-Biggs et al., 2000). We can recognize that computing the right side of Hamilton's equations (e.g., see Equation A1) involves a well-defined sequential set of elementary numerical operations. Using nothing more than the exhaustive application of the chain rule, the sensitivities of the state parameters to perturbations can be computed to machine precision by a suitable algorithm. Automatic differentiation therefore obviates the need for potentially tedious manual calculations required by the direct and adjoint methods. It has become the cornerstone for constructing neural networks.

The work described here makes use of direct variational sensitivity analysis for raytracing. This is an improvement over simple finite differencing, which suffers from the aforementioned problems, and also supports focusing calculations which are described below. (As discussed later, it is sometimes expedient to revert to simple finite differencing when caustics appear in the solution.) The direct variational method is somewhat simpler to formulate than the adjoint method while posing no greater computational burden for problems such as this one with a small number of control parameters (e.g., Nodet & Vidard, 2016). We consider an inhomogeneous, birefringent, lossy ionospheric plasma with a maximum usable frequency greater than the beacon frequencies. Details regarding the formulation of the problem and the sensitivity analysis in particular are provided in Appendix A. Some additional modeling details are described below.

2.1. Signal Power and Focusing

The power of the received signal depends on a number of factors to be addressed here and later in the study. One is the power delivered by the transmitting antenna into the radiative flux tube that terminates at the receiver. Formally, this is $P_\Omega d\Omega$ where P_Ω is the power transmitted per unit solid angle and $d\Omega$ is the differential solid angle of the flux tube. The result depends on the known transmitter power and antenna radiation pattern and on the transmit ray bearing which is estimated in the course of the raytracing analysis.

Another factor is absorption. So long as the imaginary part of the index of refraction remains small compared to the real part along the raypath, the absorption can be calculated using an elementary, approximate formula which is integrated with the others during ray tracing with little added computational cost (Jones & Stephenson, 1975). The result depends on the electron collision frequency model used (see below) and on the electron number density profile, mainly at altitudes where collisions are frequent. Power measurements can thereby be used to diagnose the state of the D and E regions, where inelastic electron-neutral collision frequencies are large even where the electron number density is comparatively small.

The third factor is the cross-sectional area of the flux tube at the receive site. Estimating this area is referred to as focusing (e.g., Budden, 1991; Nickisch, 1988; Västberg & Lundborg, 1996). Consider a radiative flux tube at the transmitter with a differential solid angle $d\Omega = \sin(\eta_t) d\eta_t d\xi_t$ where $d\xi_t$ and $d\eta_t$ are variations in the azimuth and zenith angle of the transmit ray bearing, respectively. The corresponding differential cross-sectional area of the tube at the receive antenna will be

$$dA = R^2 \cos(\eta_r) \sin(\theta) \left| \frac{\partial \theta}{\partial \eta_t} \frac{\partial \phi}{\partial \xi_t} - \frac{\partial \theta}{\partial \xi_t} \frac{\partial \phi}{\partial \eta_t} \right| d\eta_t d\xi_t \tag{1}$$

where θ and ϕ represent colatitude and longitude, respectively, R is the radial distance from the center of the earth, and η_r is the receive zenith angle. The partial derivatives in Equation 1 must be determined through sensitivity analysis. The analysis is expected to hold except near a caustic where dA vanishes and the geometric-optics limit breaks down.

Neglecting absorption, the predicted power to the receiver will be the product of the quotient $P_\Omega d\Omega / dA$ and the receive antenna effective aperture along the bearing of the incoming ray which is also known. Including absorption, it becomes possible to predict power measurements for the rays and to penalize features in the electron density model giving rise to discrepancies. Like the pseudorange and beat carrier phase observables, the power observables are enter into the optimization objective functions through least squares operators.

2.2. Electron Collision Model

A detailed analysis of ionospheric absorption and the underlying treatment of electron collisions was presented recently by Zawdie et al. (2017) who summarized practices over the last several decades. They distinguished between deviative absorption which occurs near the reflection height where rays bend drastically and non-deviative absorption which occurs well below the reflection height where rays are nearly straight but where the product of the electron number density and collision frequency can be much greater. Whereas the former is relatively consistent and relatively minor for rays that penetrate to the F region, the latter is more variable (occurring only when D and/or E layers are present) and can be much larger. For the present purposes, we neglect contributions from deviative absorption and concentrate on non-deviative absorption. We consequently neglect electron Coulomb collisions and consider only electron-neutral collisions.

Zawdie et al. (2017) point out that two formulations of the dispersion relation for ionospheric waves are in common use—the Appleton Hartree formula (Budden, 1985) and the Sen Wyller formula (Sen & Wyller, 1960). Whereas the former is a cold-plasma approximation, the latter assumes the collision frequency varies with electron energy. The former incorporates an effective collision frequency which is the monoenergetic collision frequency integrated over the electron thermal distribution. The latter incorporates the monoenergetic frequency evaluated at the most likely electron velocity (and is only defined for electron-neutral collisions). The collision frequency values to be used with the two formulations therefore differ. Zawdie et al. (2017) concluded that the two formulations predict comparable absorption rates in the D and E regions if the Appleton Hartree formula is populated with the effective collision frequency as defined, for example, by Schunk and Nagy (2009).

Below 150–200 km altitude, the most important electron neutral momentum transfer collisions are with molecular nitrogen and molecular oxygen with rates that depend on the density of each species along with the electron temperature. Collisions with atomic oxygen become increasingly important with increasing altitude. The effective electron neutral collision frequency can be calculated using neutral densities taken from the NRLMSISE00 empirical model and the formulas provided by Schunk and Nagy (2009). The result can be represented accurately by a simple bi-exponential function (e.g., Settimi et al., 2015). A bi-exponential electron-neutral collision frequency calculated for the appropriate latitude, longitude, local time sector, and F10.7 cm solar flux level is used for our analysis.

2.3. Electron Density Profile Shapes

A simple parametrization of the electron density profile is required for the forward model. Chapman profiles are a natural choice, being the foundation for analytic solutions of actual profile shapes under certain simplifying assumptions. The Chapman profile is defined by four parameters: the peak electron number density, the peak height, and the scale height which can differ in the bottomside and topside (i.e., the profile can be composed of two Chapman functions with different scale heights made to be piecewise-continuous just above the peak.) Chapman profiles could be superimposed to represent multiple ionospheric layers

Studies have pointed to other parametrizations which can reproduce actual ionospheric density profiles with smaller residuals, however. Nava et al. (2008) discuss parametrizations based on semi-Epstein layers which are also defined by a peak number density, peak height, and distinct bottomside and topside scale-height controls. An important distinction is that the topside scale height varies in a prescribed way.

Either Chapman or semi-Epstein layers can be used in the existing forward model. In this study, we describe the F region with a four-parameter Chapman layer. The model also has the provision to add an E layer with a Chapman or semi-Epstein layer with one free parameter, the peak density. This is a reasonable simplification given that the shape of the equatorial E layer has been found to be relatively invariant (Hysell & Chau, 2001). In the interest of simplicity, there is no E layer in this study, however. This is a reasonable simplification in the postsunset sector.

The model also has provisions for a simple D layer which should sometimes be detectable in the signal power observable at twilight. Cummer et al. (1998) present a two-parameter D-region parametrization that could be added with relatively light additional computational burden. A four-parameter model developed by McCormick (2019) improves upon the two-parameter model by representing the split that occurs in the daytime. The computational burden of the improved model is significantly higher, however. For this study, we incorporate a simple Gaussian layer with a five-kilometer half width and a peak height of 85 km.

2.4. B-Spline Horizontal Interpolation

The electron number density model is extended to three dimensions with the use of B-splines (e.g., De-Boor, 1978) in the manner outlined by M. L. Psiaki et al. (2015). The five coefficients defining the aforementioned profile shapes are each expanded in the form of either bicubic or biquintic B-splines. These are families of polynomials with weights that are prescribed at certain nodes on a grid. B-splines of degree n have continuous derivatives through n-1. The functions and their first and second derivatives are tabulated within the algorithm. We use a two-dimensional grid in latitude and longitude with uniformly spaced nodes spanning the region where the beacons are deployed. The work presented here makes use of biquintic B-splines on a 15×15 grid, implying a total of 1125 parameters.

2.5. Numerical Quadrature

The sensitivity equations are stiffer than the ordinary raytracing equations. Whereas any number of quadrature methods would be suitable for integrating the latter, including adaptive methods, the former require methods specially designed to handle stiff systems. Here, we utilize an extrapolation method based on the linearly implicit midpoint rule of Bader-Dueflhard described by Hairer and Wanner (1990).

2.6. Objective Function

The optimization routine minimizes in the least squares sense an objective function composed of a number of penalties. The penalties include discrepancies between model predictions and experimental observables

Table 1
HF Beacon Station Locations

Station	Latitude (north)	Longitude (east)	Altitude (masl)
Jicamarca	−11.950	−76.873	52
Huancayo	−12.042	−75.323	3119
Mala	−12.666	−76.628	31
La Merced	−11.126	−75.368	817
Barranca	−10.760	−77.760	55
Oroya	−11.551	−75.942	3790
Ancon	−11.777	−77.150	51
Sicaya	−12.040	−75.296	3330
Ica	−14.089	−75.736	402

Note. Receive (transmit) stations are above (below) the line.

from the HF network, the group delay, accumulated Doppler phase, and power, namely. Given three transmitters, six receivers, and two frequencies, there are 36 rays and 108 penalties (36 rays times three observables) to consider here.

Additional penalties are derived from electron density profiles measured by the Jicamarca incoherent scatter radar or the ionosonde. GPS-TEC measurements from a receiver at Jicamarca are also incorporated in the electron density recovery algorithm. TEC estimates are computed from the electron density model by integrating along the bearing to the satellite. Model-data discrepancies are then incorporated in the global optimization problem through penalties. Only PRNs with elevation angles greater than 60° were considered, and then no more than three PRNs at any given time. Penalties are made to be small when the geometry and satellite zenith angle are such that the TEC estimates are influenced significantly bt electron densities outside the reconstructed ionospheric volume.

The objective function also includes penalties used to introduce regularization. The electron density model is mixed determined and poorly conditioned, and regularization is required for stability. We penalize the curvature in the horizontal direction of the five parameters that control the electron density representation. This prevents the production of spurious model features lacking support in the data.

The objective function is minimized using a Levenberg Marquardt algorithm. The computation is parallelized, with raytracing for each ray handled by a separate processor. Ray shooting also takes place within a Levenberg Marquardt algorithm with the Jacobian matrix supplied through sensitivity analysis.

3. Data Presentation

An HF beacon network consisting of three transmit and six receive stations has been deployed in Peru in the vicinity of the Jicamarca Radio Observatory for specifying the ionospheric electron density regionally with the goal of forecasting plasma instability associated with ESF. The transmitters operate at two frequencies, 2.72 and 3.64 MHz, and utilize distinct pseudorandom codes with baud widths of 10 μs and repetition times of 0.1 s, giving a compression ratio of 10,000. The transmitter power is ∼10 W. Dipole antennas are used for transmission and reception. The observables from the receivers include pseudorange, Doppler shift or accumulated carrier phase, and power at a cadence of once per minute. Technical details regarding the network were given by Hysell et al. (2018). The locations of the transmitters and receivers are shown in Table 1.

We present data from two nights of observation. The first night is June 10, 2019. ESF occurs rarely in the postsunset interval in the Peruvian sector in June (e.g., Chapagain et al., 2009) and did not occur in the interval of interest here between 1900 and 2200 LT. It did occur later, near midnight, as is common during periods of very low solar flux (see Otsuka, 2018 for review).

The motivation for examining these particular data are evident in Figure 1 which shows pseudorange and accumulated carrier phase data for all 18 3.64 MHz ray paths covered by the network. Our convention for plotting is to define the pseudorange as $c\tau / 2$ where τ is the time of flight of the signal. The accumulated Doppler phase is the time integral of the Doppler velocity in m/s, $v = \omega / k$, where ω is the Doppler frequency and k is the scattering wavenumber $(4\pi / \lambda)$. (Note that these conventions are used for plotting because they facilitate comparisons with data from monostatic radar to some degree. For analysis, the pseudorange is $c\tau$, and the Doppler velocity involves the wavenumber $(2\pi / \lambda)$.) An arbitrary offset is added to the accumulated carrier phase so that the curves can be plotted on the same axes as the pseudorange.

The figure depicts a gradual increase in pseudorange and accumulated carrier phase for all the ray paths after 1900 LT. This is a common feature of data from the network and reflects the rise of the postsunset F layer due to a combination of proper motion and recombination. More remarkable are the unusually distinct quasi-periodic variations in all the curves. The variations have periods of 20–30 min and may be indicative

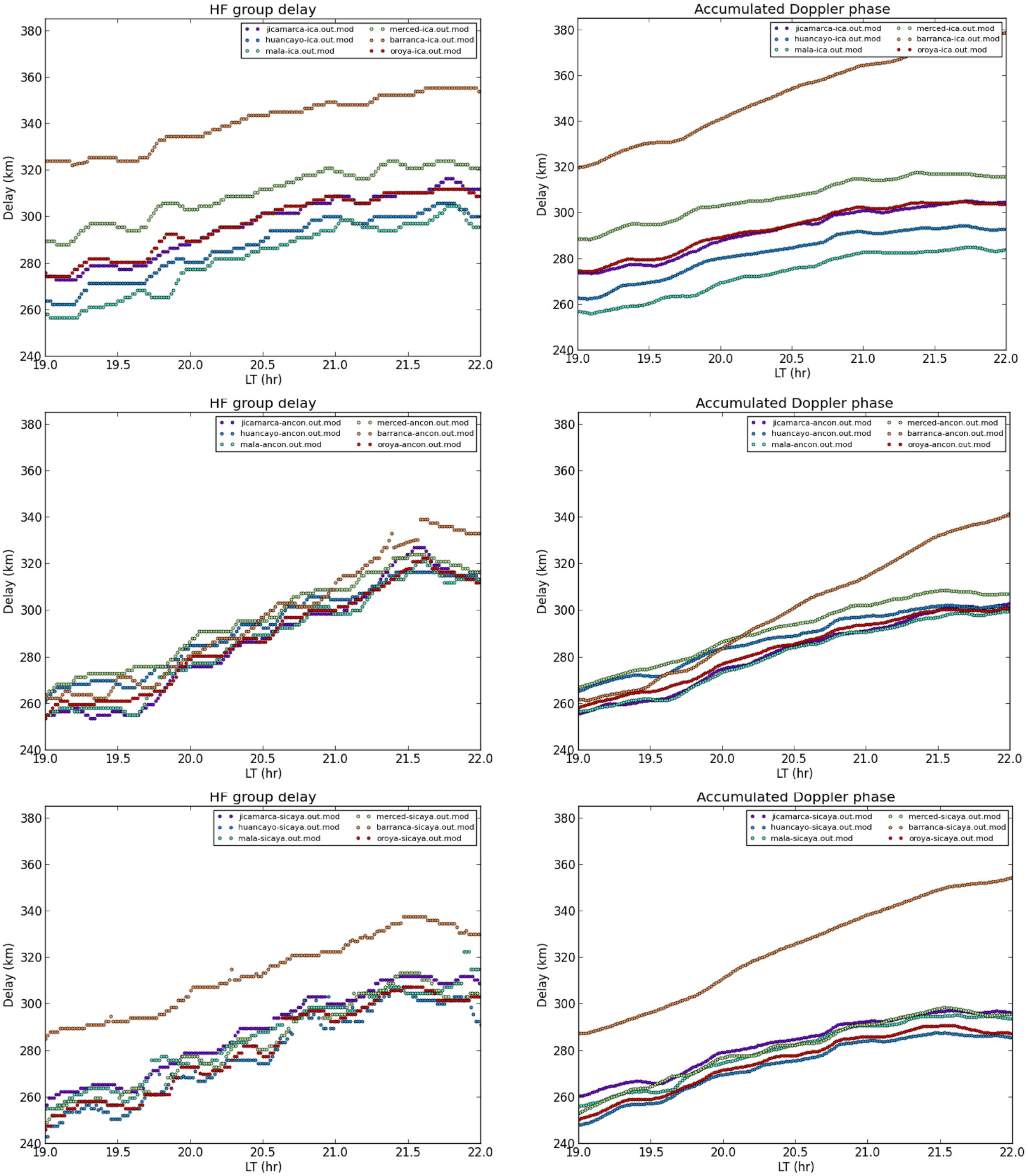

Figure 1. Group delay (left) and accumulated carrier phase (right) measurements versus local time on June 10, 2019 for 3.64 MHz. The top, middle, and bottom rows represent signals transmitted from Ica, Ancon, and Sicaya, respectively. The six curves in each panel represent signals received at six different receive sites as indicated.

of medium-scale traveling ionospheric disturbances. Capturing them in numerical simulations could be an important part of an ESF forecast strategy.

Similar variations are not clearly evident in the HF data for 2.72 MHz (not shown). They are likewise not especially clear in the signals from the transmitter at Ica. Ica is the southernmost station in the network and the transmitter most distant from the receivers. The variations are more distinct in the signals transmitted from Ancon and Sicaya which involve shorter, higher elevation paths. Overall, the rays with the highest turning points are the ones with the strongest quasiperiodic variations. The variations are furthermore much more distinct in the pseudorange observables than in accumulated carrier phase. That the phases of the fluctuations in different ray paths can differ indicates that their dominant physical scale sizes are not very long compared to the distances between the stations. That the amplitudes and periods of the fluctuations vary in time and between ray paths argues that one or more wave packets as opposed to a single, coherent, monochromatic wave were at work.

The Jicamarca incoherent scatter radar was not operating on June 10, 2019. Data from the Jicamarca ionosonde are available for supplementing the HF data, however. Also available are TEC estimates from a GNSS receiver deployed at Jicamarca by the Satellite Navigation and Sensing Laboratory at the University of Colorado Boulder. The TEC data were derived using an algorithm which simultaneously estimates the TEC and receiver hardware bias based on measurements from a single receiver (Bourne, 2016; Bourne et al., 2016).

Figure 2 depicts the volumetric electron density reconstructed in the Peruvian sector from the HF pseudorange and Doppler-shift data together with GPS measurements and soundings at 15 min intervals from the ionosonde at Jicamarca. The figure shows isodensity contours for 10^{10} and 10^{11} m^{-3}, respectively. The cadence for the method is once per min, and reconstructions are shown here at 30 min intervals.

Three main features are evident in the reconstructions. First, the bottomside F layer is seen to ascend slowly throughout the interval. Second, there is a modest meridional tilt in the isosurfaces which could be telltale of the development of the Appleton anomaly to the south of the dip equator which is at approximately −12° latitude. Third, a distinct zonal tilt on the layer height emerges during the interval shown. The tilt could be the result of local convection or the advection of a deformed bottomside through the field of view. Radar data from Jicamarca shown below will be suggestive of the latter scenario.

Figure 3 shows a comparison between the GPS measurements from Jicamarca (crosses) and model predictions (circles), with different colors assigned to different PRNs. As GPS TEC offers the only constraint on the model topside ionosphere scale height in this case, the good agreement merely means that the topside scale height estimates could be fairly uniform across the region while maintaining consistency with the satellite data.

In addition to the coarse structure evident in Figure 2, the HF reconstruction method can also capture relatively fine structure in the electron density. We show this by inspecting the shapes of isodensity curves calculated at different times. Figure 4 shows the relative vertical displacements of the $N_e = 10^{11}\ \mathrm{m}^{-3}$ isosurface. Before plotting, we fit and subtracted the quadratic trend in the surface height to remove as much of the gross structure already evident in Figure 2 as possible. The result shows residual wavelike variations in layer height across the region. The variations are mainly zonal but also partly meridional.

Over time, the features seen in Figure 4 propagate slowly to the east for a time before coming to rest. The amplitude of the features, as measured by the difference between the highest crest and lowest trough, varies periodically, however. The period is ∼30 min. Figure 4 was computed at 1950 LT when the amplitude was a maximum. The periodicity is similar to that seen in the raw data in Figure 1. Overall, the model suggests the presence of spatial fluctuations in layer height which are not propagating but which are waxing and waning periodically. Changes in layer height cause variations in the pseudoranges of the rays mainly by inducing tilts away from great-circle paths.

The JULIA coherent scatter radar at Jicamarca was operating on June 10, 2019, and the observations are represented in RTI format in Figure 5. The brightness of the image pixels is proportional to the signal-to-noise ratio on a dB scale. The hue represents Doppler shift, with blue (red) tones implying motion toward (away from) the radar on a scale spanning ± 100 m/s. The saturation of the pixels represents Doppler width, with pure (pastel) colors signifying narrow (wide) spectra.

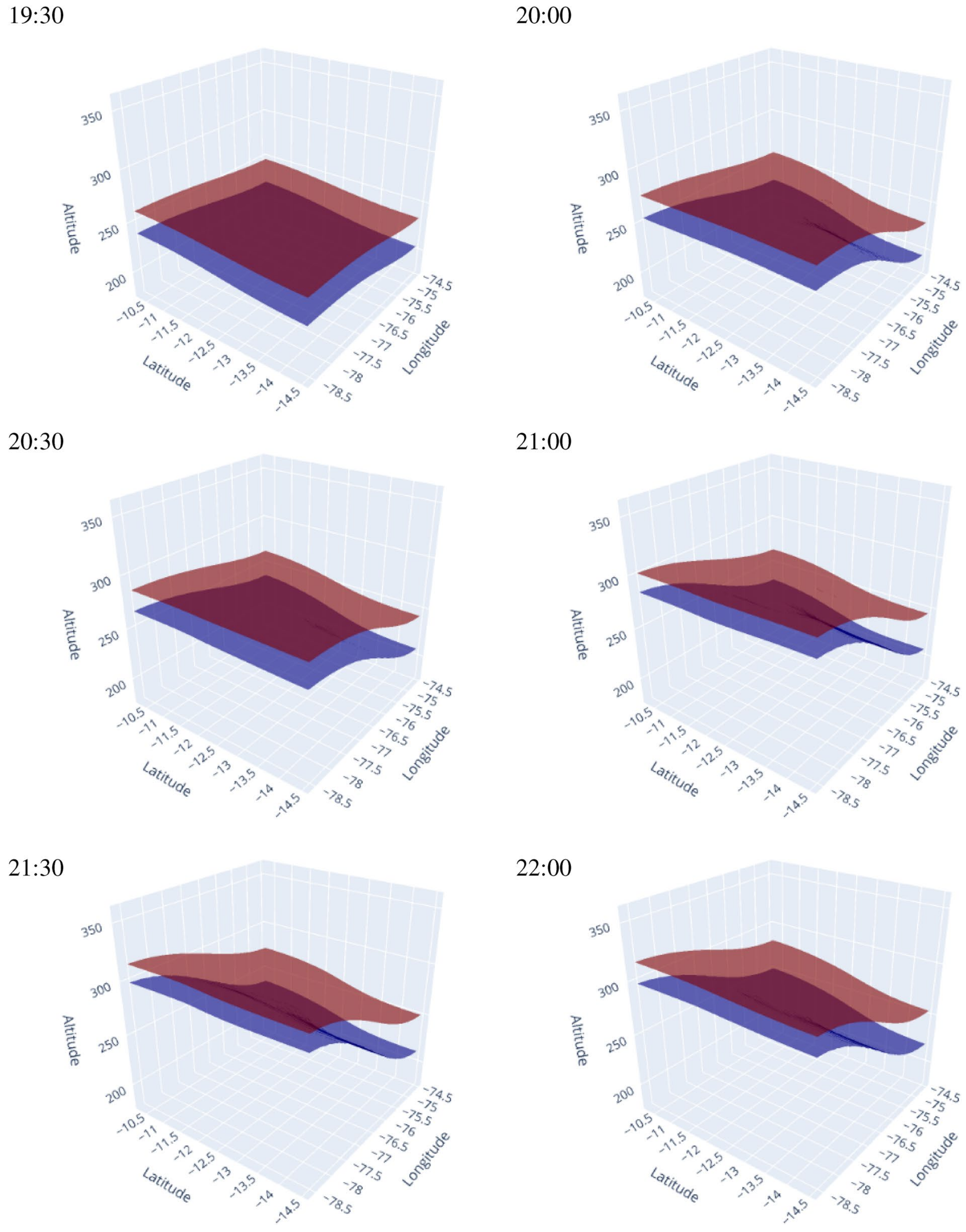

Figure 2. Reconstructed electron density isosurfaces generated from high-frequency pseudorange and Doppler-shift data over a period of three hours on June 10, 2019. The blue (red) surfaces represent $N_e = 1 \times 10^{10}$ and 1×10^{11} m^{-3}, respectively.

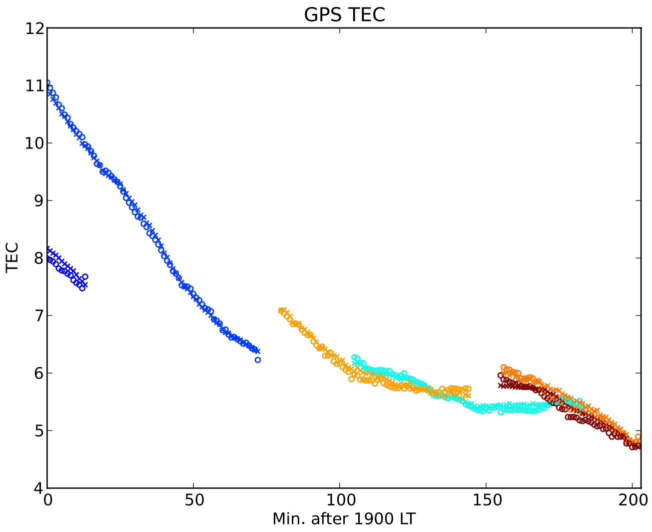

Figure 3. Figure showing measured (crosses) and modeled (circles) GPS TEC values for six pseudo random noise (PRNs) passing through the region. Different colors are assigned to different PRNs.

Figure 5 is typical in some respects for ESF events observed at Jicamarca. A narrow bottom-type scattering layer at about 250 km altitude evolved after about 2330 LT into a series of vertical plumes characteristic of plasma interchange instability. Results from interferometry and radar imaging (now shown) indicate that the flow was mainly eastward over the radar during the event, although shears were sometimes present, and the bottom-type layer drifted very slowly.

The most remarkable aspects of the ESF event were its occurrence in June, an unfavorable season for ESF in the Peruvian sector (Chapagain et al., 2009; Hysell & Burcham, 1998), and its late onset time, which was well after sunset. The HF electron density reconstructions suggest a scenario in which a large-scale bottomside deformation advected over the radar, causing the layer to to appear to rise, plateau, and then fall overhead. Such a deformation would be conducive to ionospheric interchange instability, which has a growth rate that increases with altitude, and to the clustering of irregularities in the vicinity of the deformation (Hysell et al., 2020). Additionally, the fine structure evident in Figure 4 could be interpreted either as a seed for instability or evidence of instability underway.

The next data set considered here is from December 3, 2019. The JULIA RTI plot for the event is shown in Figure 6. This event was characterized by a narrow bottom-type scattering layer emerging at 2000 LT that turned to a more vertically developed bottomside layer at about 2130 and then a small topside radar plume that passed overhead at about 2330 LT.

The Jicamarca incoherent scatter radar reported very small vertical plasma drifts prior to 2000 LT and no prereversal enhancement. Starting at 2000 LT, the drifts began increasing approximately linearly, reaching about 10 m/s by 2130 LT by the time small plumes began passing over the radar. Zonal Pedersen currents associated with vertical drifts are the main drivers for the collisional interchange instability. The small plumes are likely a direct consequence of the late ascent of the layer.

The pseudorange and carrier phase data for the December 3, 2019 event are shown in Figure 7 for the sake of completeness. These were qualitatively similar to those from June 10, 2019, only with less clear quasiperiodic variations and with smaller increasing trends overall.

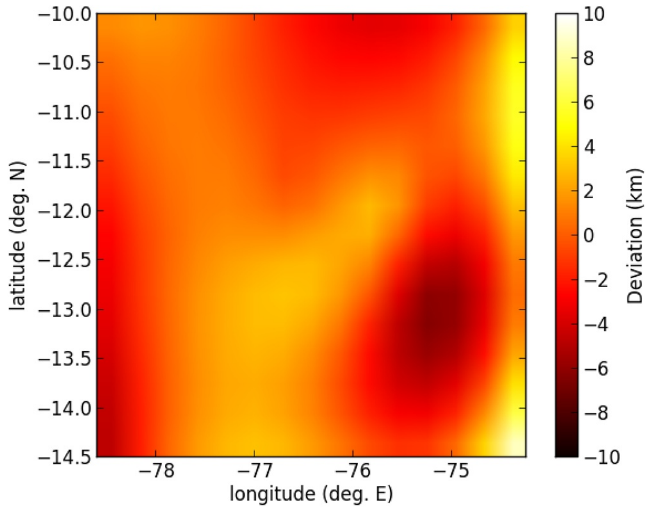

Figure 4. Fine structure in reconstructed electron isodensity surface height at 1950 LT (see text).

In addition to these observables, the relative power associate with the first hops for all the links in the December 3 HF data was also calculated. Representative examples are given in Figure 8 which shows relative signal power (averaged over a minute) for all the links involving the HF receiver at Jicamarca. Noise and, to the greatest extent possible, interference have been removed from these estimates by clipping the amplitude prior to summing the power in all range and Doppler bins into which the first-hop signals fell.

The signals exhibit considerable small-scale variability or fading which is superimposed on large-scale, gradual arcs. Fading at medium and high frequencies has been investigated since the early days of radio—see Salaman (1962); Davies (1965); Rao et al. (2002); Bianchi et al. (2013) and references therein for reviews. The causes of fading include time-variations in absorption and focusing as discussed above. Closely related to focusing is multipath propagation. Magneto-ionic effects can also cause fading, specifically when the X and O modes are mixed, leading to Faraday rotation and the possibility of time-varying polarization mismatch with linearly polarized antennas used for reception.

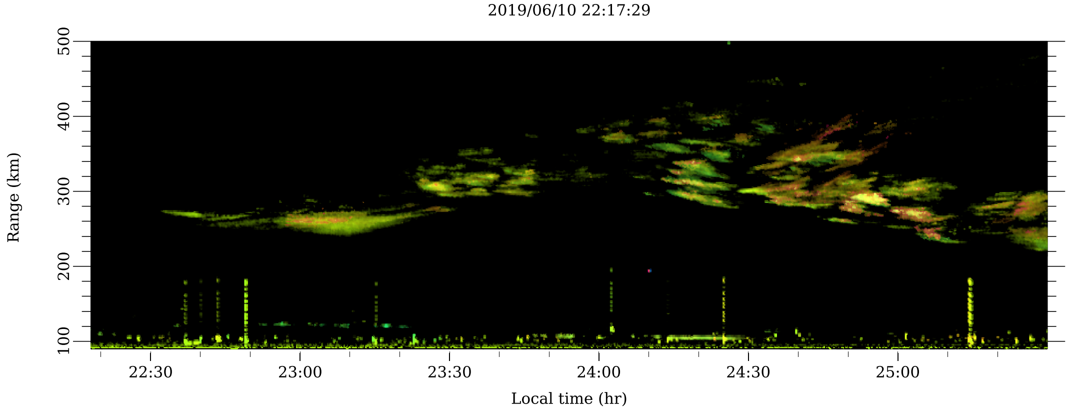

Figure 5. Jicamarca range-time-intensity representation of coherent scatter from equatorial spread F irregularities observed on June 10, 2019.

Multipath and polarization fading at HF normally exhibits timescales of a few seconds or less and so should not contribute significantly to the power measurements used here. Focusing and absorption, meanwhile, should contribute mainly to fading with timescales of tens of minutes or more. It is these phenomena about which inferences will be made.

Finally, scintillation can also cause fading. While the purpose of this investigation is to characterize the F region ionosphere before the onset of ESF and the attendant scintillations, plasma density irregularities are ever present in the equatorial electrojet, and HF signals have been shown to be strongly affected by them, particularly during the day but also at night (Woodman et al., 2006). The Fresnel scale for HF signals in the E region is of the order of 2 km which is comparable to the wavelength of large-scale gradient drift waves in the electrojet (Kudeki et al., 1982). The periods of these waves is tens to hundreds of seconds. Scintillations likely contribute significantly to the small-scale fading in the HF data.

To incorporate the HF power observables in the analysis, we represent them with a fifth-degree polynomial fit calculated over the analysis period, 1815–2045 LT in this case. The fit curves show power levels that peak broadly between about 1830–1930 and that decrease thereafter. The curve shapes differ between the two HF frequencies and from station to station, with peaks occurring earlier in the signals from Ancon than in those from Ica and Sicaya. This would seem to indicate spatial variations in the F layer morphology/curvature. Since the power measurements are relative rather than absolute and calibrated, we normalize them to the predicted ray powers at a time after sunset when the isodensity surfaces at the magnetic equator are presumed to be nearly flat and regular. The modeling then accounts for power variations which occur

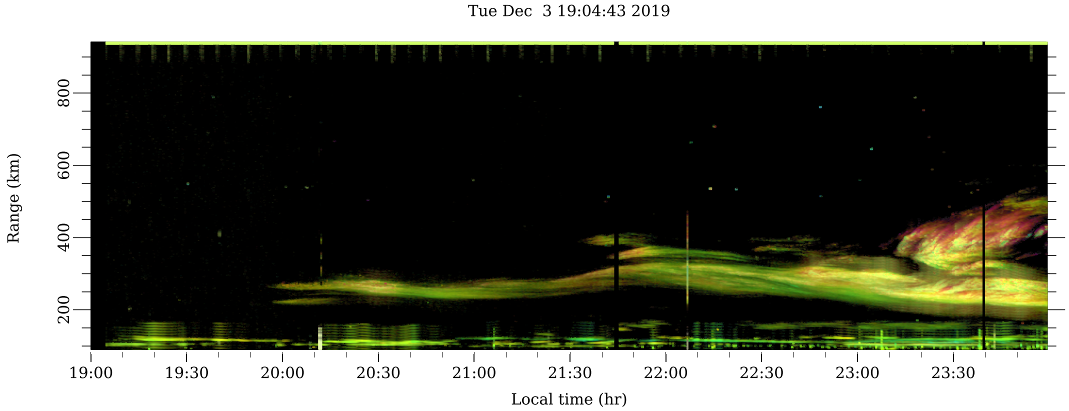

Figure 6. Jicamarca range-time-intensity representation of coherent scatter from ESF irregularities observed on December 3, 2019.

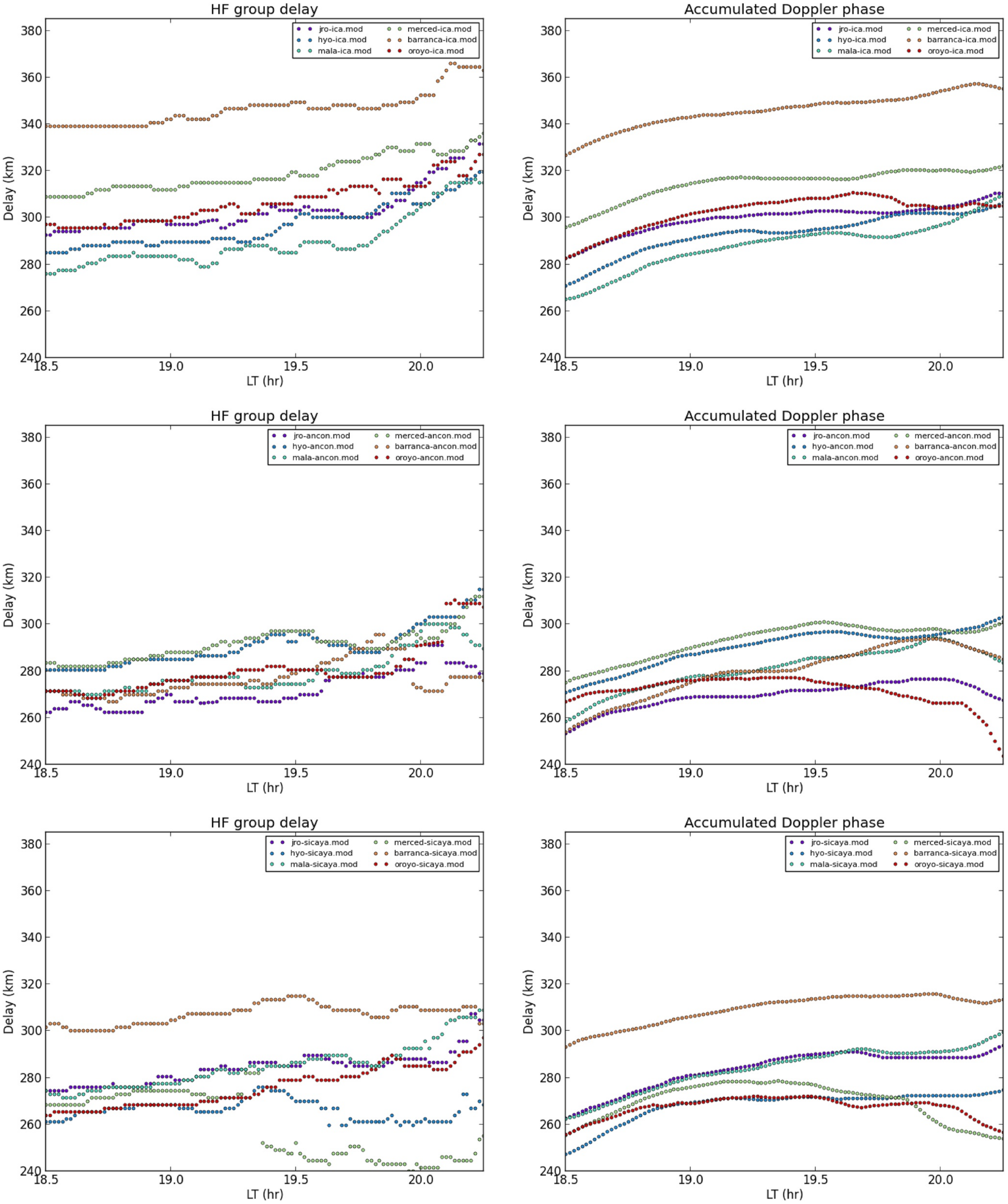

Figure 7. Group delay (left) and accumulated carrier phase (right) measurements versus local time on December 3, 2019 for 3.64 MHz. The top, middle, and bottom rows represent signals transmitted from Ica, Ancon, and Sicaya, respectively. The six curves in each panel represent signals received at six different receive sites as indicated.

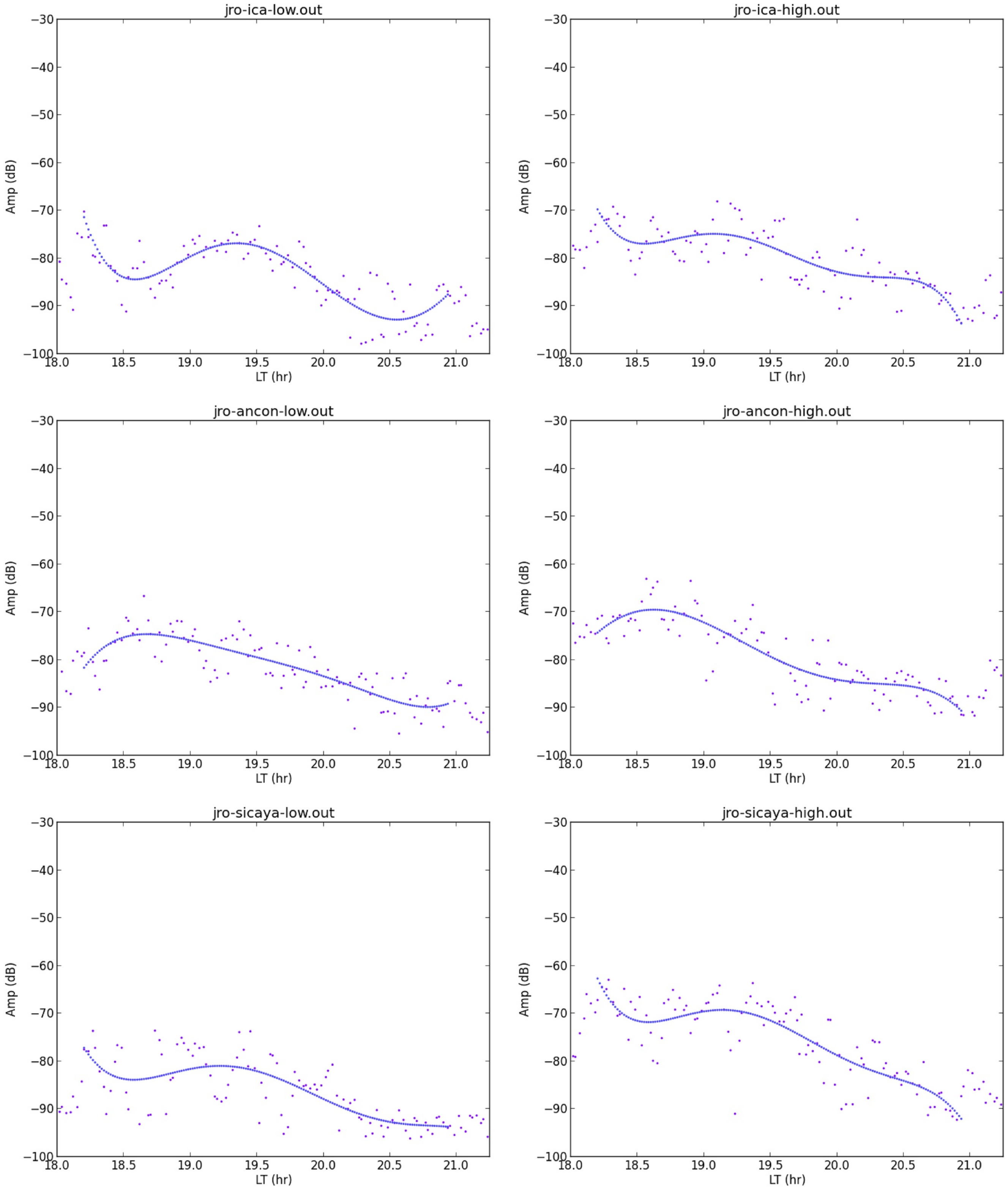

Figure 8. Relative received signal power estimates for the Jicamarca receiver on December 3, 2020. Here, "low" and "high" refer to frequency, 2.72 and 3.64 MHz, respectively. Smoothed fits to the data are used for subsequent analysis.

subsequently. This is a preliminary approach which will be update once a means of calibrating the received signal power has been developed.

Note that variational sensitivity analysis can be problematic when caustics emerge in the model N_e field. Caustic isosurfaces are ellipsoidal cylinders aligned with the raypath. When they emerge, the sensitivity terms go to zero, and iteration over ray bearing may stop prematurely. We have found that the problem can be remedied by reverting to brute-force (finite difference) sensitivity analysis on the occasions when convergence fails. Finite differencing dislocates the pilot rays from the small caustic surfaces sufficiently for convergence to occur.

Figure 9 shows reconstructed electron density isosurfaces from December 3, 2019, between 1845 and 2000 LT. The bottomside F region was evidently steeper on this date than on June 10, 2019, and ascended much more gradually. There is no indication in the December 3, 2019, isosurfaces of large-scale bottomside perturbations especially conducive to interchange instability. The relatively steep bottomside combined with the period of plasma ascent detected by the Jicamarca ISR prior to 2130 therefore remain the most plausible explanations for the modest plumes that erupted eventually from the bottomside scattering layer seen in Figure 6.

The most important aspect of the isosurfaces in Figure 9 is their changing curvature. The isosurfaces went from being slightly concave at 1845 LT to significantly concave between 1900 and 1915 LT to nearly flat again at 1930 LT to convex thereafter. The curvature changes together with the gradual ascent of the F layer are broadly consistent with the relative power levels shown in Figure 8 which peaked early in the event (at different times for different ray paths) and then decreased as time progressed.

In this analysis of postsunset data, the modeled peak D-region density was estimated to be fairly uniform and very small, between 5 and 10×10^8 m^{-3} mainly, and too small to contribute significantly to absorption. Daytime beacon experiments are generally precluded at Jicamarca by reflection and scattering from the E region, and there is only a small postsunset window when the D region can be an important factor in the ray power budget (see for example Reyes et al., 2020). Data from within this window were not available in the present data set. Future experiments will target the estimation of D-region densities before the D region has recombined.

4. Analysis

Postsunset ESF is rare during June solstice in the Peruvian sector but occurred (albeit well after sunset) on June 10, 2019, when the HF high-band pseudorange data also exhibited unusually distinct quasiperiodic fluctuations. The event was characterized by a large-scale zonal deformation in the F-layer height which appeared to advect eastward gradually throughout the event. The horizontal scale of the perturbation was at least several hundred kilometers which is too large to be a direct result of collisional interchange instability (Zargham & Seyler, 1987). A more likely explanation for the structuring is neutral atmospheric forcing which encompasses these scales. The ionospheric deformation indicated in Figure 2 was significant, with the crest of the deformation being about 100 km higher than the trough. Deformation affects ionospheric stability, the interchange instability growth rate increasing universally with altitude and with decreasing ion-neutral collisions. Depletion plumes would have been more likely to form at the crests of deformations. The morphology of the coherent scatter in Figure 5 is consistent with this scenario for ESF formation.

In addition, periodic fine structure with a horizontal wavelength of approximately 100 km was superimposed on the large-scale structuring. The fine structure was static rather than propagating and waxed and waned in amplitude with a 30 min period. While the ionospheric interchange instability can operate at 100-km wavelengths, and while waves can be stationary in the bottomside where the zonal flow exhibits strong shear, periodic amplitude variations suggest a different root cause. Hysell et al. (2014) simulated the response of the equatorial ionosphere to thermospheric waves propagating upward from turbulent regions in the mesosphere with horizontal wavelengths of about 100 km. The waves drove undulations in the bottomside ionization that also waxed and waned with the gravity wave period. As the neutral waves could not remain in phase with the bottomside undulations, the effect was for the former to repeatedly create and

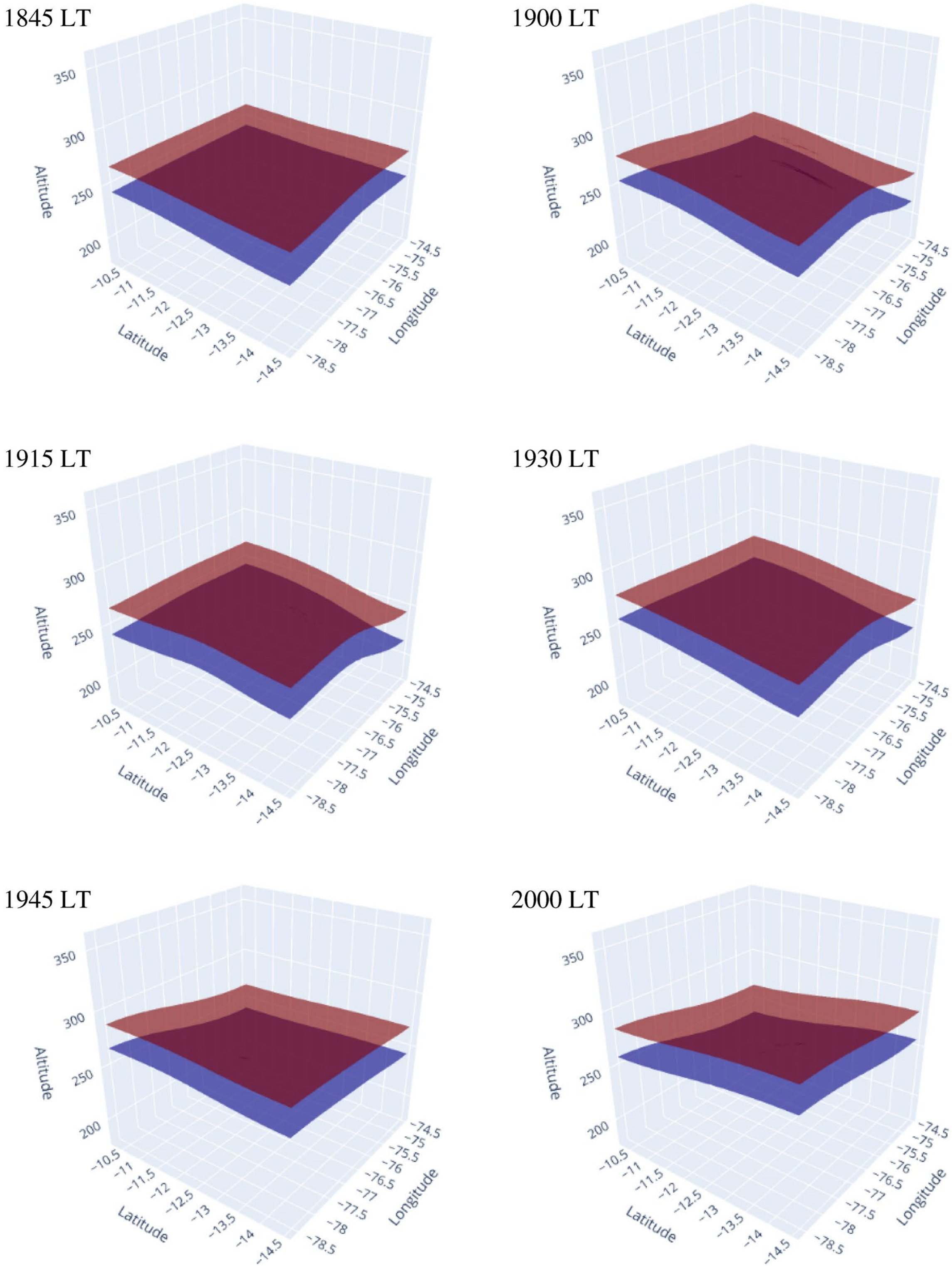

Figure 9. Reconstructed electron density isosurfaces generated from high-frequency pseudorange, Doppler-shift, and power data over a period of 75 min on December 3, 2019. The blue (red) surfaces represent $N_e = 1 \times 10^{10}$ and 1×10^{11} m^{-3}, respectively.

destroy the latter. The ionospheric interchange instability was not seeded by the gravity waves in simulation in this case. We do not know what role the fine structure played in the occurrence of ESF on June 10, 2019.

Postsunset ESF is climatologically more likely to occur in December solstice than June solstice, and the modest ESF event observed on December 3, 2019, was neither unusual nor anomalous, particularly in view of the small but finite vertical plasma drifts that occurred late in the event. A numerical simulation (not shown) of the event conducted in the manner of Hysell et al. (2015) using ISR data alone predicted the emergence of small depletion plumes late in the event before midnight. Data from the HF network would not have improved the fidelity of the forecast in this specific case.

5. Conclusions

HF data sets from June to December solstice during very low solar flux conditions were analyzed using a constrained optimization method to estimate the ionospheric electron number density regionally in three-dimensional (3D). The method incorporates the HF observables (pseudorange, beat carrier phase, and signal power) as well as data from GPS receivers, an ionosonde, and the Jicamarca incoherent scatter radar when those data are available. The regional electron density estimate is initialized shortly after sunset when the F region ionosphere is typically nearly horizontally uniform. Thereafter, the estimate is updated once per minute.

Sensitivity analysis using direct variational methods was added to the recovery algorithm. Sensitivity analysis improves stability overall and permits the interpretation of HF signal power as an additional observable. The signal power is indicative of both the bottomside F region morphology and of absorption along the ray paths. Measuring it therefore helps the recovery problem, which is strongly underdetermined, and offers a means of measuring ionization below the F layer which can contribute to absorption before sunset. Note that D- and E-region density profiles cannot be measured at Jicamarca due to clutter from irregularities in the mesosphere and the electrojet (Reyes et al., 2020). Variational sensitivity analysis can fail when caustics occur in the model ionosphere. In such cases, a fallback method employing brute-force (finite difference) sensitivity analysis proves to be more robust.

On both occasions considered, modest ESF events characterized by small radar plumes were observed well after sunset. Traditional forecasts using DNS based solely on incoherent scatter measurements at zenith would not have predicted ESF in the June 10, 2019, event given the absence of significant postsunset uplift. The analyzed HF data point to a large-scale background electron density deformation that would have been difficult to infer from a vertical-pointing ISR and that presumably contributed to instability. Fine structure seen in the HF analysis also suggests forcing that would be conducive to instability. Since the goal of this work is to make inferences from the HF data to inform DNS forecasts of ESF, we regard these findings as a validation of the methodology. The fine structure in particular would not have been detectable using the less mature network of stations described by Hysell, Baumgarten, et al. (2018).

The most significant finding from the December 3, 2019, HF experiments is that signal power measurements are broadly consistent with and can be used to help constrain the morphology/curvature of the bottomside F region. Utilizing all available observables is important in view of the fact that the recovery problem is strongly underdetermined. Moreover, the D-region density recovered from the analysis was plausible and stable. Future experiments spanning sunset will be necessary to validate the methodology going forward.

The HF beacon sites are distributed geographically according to the availability of ground sites. The distribution affects the spatial resolution of the ionospheric recovery. Fine structure at the scale of ∼100 km can be recovered by the existing network. This extends into the range of wavelengths at which the ionospheric interchange instability operates, meaning that the HF data can be used not only to initialize and constrain the background conditions for DNS simulations but also to seed them.

It would be straightforward to use ionospheric recoveries like those in Figures 2 and 9 to initialize 3D DNS simulations of ESF. This would be superior to the approach followed now by Hysell et al. (2015) which is to initialize them using empirical and physics-based models tuned to match Jicamarca observations assuming an equivalence between local time and longitude. Another, more comprehensive forecasting approach would be to assimilate the HF data directly. While we plan to attempt this, the computational cost is likely to be quite high based on our experience with the comparatively simple constrained optimization problem being solved presently.

Appendix A: Direct Variational Sensitivity Analysis

Here, we provide details regarding sensitivity analysis in the raytracing methodology. The analysis begins with the augmentation of the equations used for updating the raytracing state vector. The state vector includes the coordinates and their conjugate momenta at points defining the ray, that is, in spherical coordinates, $p = (k_r, k_\theta, k_\phi, r, \theta, \phi)$. Other parameters may be added to the state vector, for example, the phase path length and power, but only these six are required for raytracing.

The raytracing equations are Hamilton's equations for the Hamiltonian $H(p,\omega,t)$. They can be derived from the Euler Lagrange equations and the application of variational mechanics to Fermat's principle. The result is a system of coupled differential equations of the form (see Equations 9–14 in Jones & Stephenson, 1975):

$$p_i' = f_{1i}(r,\theta)\frac{1}{c}\frac{H_{p_j}}{H_\omega} + f_{2i}(r,\theta,k_\theta,k_\phi,p') \tag{A1}$$

where $p_i' \equiv dp_i / dP$, $P = ct$ is the group path length, $H_{p_j} \equiv \partial H / \partial p_j$ and $H_\omega \equiv \partial H / \partial \omega$ denote components of the gradient of the Hamiltonian, and where f_{1i} and f_{2i} arise from the metric tensor for spherical coordinates. Also, p_i is conjugate to p_j. The Hamiltonian is based on an invariant quantity along a raypath and can be expressed in a number of ways (see below). For the present purposes, the Hamiltonian is taken to be time invariant. At every step, the equations are solved using numerical quadrature.

The corresponding equations describing the sensitivity of the state vector to a control parameter λ therefore take the form (noting that the prime and the $\partial / \partial\lambda$ operators may be interchanged):

$$\left(\frac{\partial p_i}{\partial \lambda}\right)' = f_{1i}(r,\theta)\frac{1}{c}\frac{\left\{H_{p_j}, H_\omega\right\}}{H_\omega^2} + \left(\frac{1}{c}\frac{H_{p_j}}{H_\omega}\frac{\partial f_{1i}}{\partial p_k} + \frac{\partial f_{2i}}{\partial p_k}\right)\frac{\partial p_k}{\partial \lambda} + \frac{\partial f_{2i}}{\partial p_k'}\frac{\partial p_k'}{\partial \lambda} \tag{A2}$$

where we employ the notation

$$\left\{H_{p_j}, H_\omega\right\} \equiv \left(H_\omega H_{p_j,p_k} - H_{p_j} H_{\omega,p_k}\right)\frac{\partial p_k}{\partial \lambda}, \tag{A3}$$

where H_{p_j,p_k} and H_{ω,p_k} denote components of the Hessian of the Hamiltonian, and where the Einstein summation convention is used throughout. Note that the six equations have the same form for any control parameter. The difference lies just in the initial conditions for $\partial p_i / \partial \lambda$. Using the ray bearing as control parameters, for example, the initial conditions are just the derivatives of the initial wavevector with respect to azimuth and elevation with wavenumber held constant.

The new equations augment the original ones and are evaluated in the same numerical quadrature, only now with six additional equations per control parameter. Each equation like Equation A2 contains terms on the right side of the form $\partial p_k / \partial \lambda$ which are available for computation, having been evaluated through numerical quadrature up through the current point on the ray. Since f_{2i} may contain p', there may be additional terms of the form $(\partial p_k / \partial \lambda)'$ on the right side of Equation A2 as well. However, such terms appear only in the sensitivity equations for the momenta (k_r, k_θ, k_ϕ) and involve only the coordinates (r, θ, ϕ). If the sensitivities for the coordinates are calculated first at each point on the ray, the information required for the momenta sensitivities, which are calculated next, will be available explicitly.

The Hamiltonian used for calculations here is the dispersion relation for the waves:

$$H = \Re\left\{\frac{1}{2}\left(\frac{c^2 k^2}{\omega^2} - n^2(p,\omega)\right)\right\}$$

The gradient and Hessian of the Hamiltonian can be calculated readily from the gradient and Hessian of the square of the index of refraction. For the latter, we utilize the Appleton Hartree equation:

$$n^2(X,Y_l,Y_t,Z) = \frac{1 - iZ - X}{2(1 - iZ)(1 - iZ - X) - Y_t^2 \pm \sqrt{Y_t^4 + 4Y_l^2(1 - iZ - X)^2}} \tag{A4}$$

in which the ± sign distinguishes between the ordinary and extraordinary mode. This formula is posed compactly in terms of the magneto-ionic parameters $X \equiv \omega_p^2 / \omega^2$, $Y \equiv \Omega_e / \omega$, and $Z \equiv \nu_{en} / \omega$. Furthermore, we have the longitudinal and transverse components

$$\begin{aligned} Y_l &\equiv Y\hat{k} \cdot \hat{b} \\ Y_t &\equiv \sqrt{Y^2 - Y_l^2} \end{aligned}$$

The gradients and Hessians of Equation A4 in terms of the four magneto-ionic parameters are somewhat involved but can be calculated expediently with the aid of computer algebra.

The $X(r,\theta,\phi)$ parameter contains the spatial dependence on electron-density that is, central to the experimental method. The most complicated parameters are $Y_t(p)$ and $Y_l(p)$ which introduce anisotropy into the problem and which depend both on the wavevector and on the magnitude and direction of the magnetic field. The Z dependence contains electron-neutral collisions which render a prediction of absorption. We take $Z = Z(r)$ here to simplify the calculations, presupposing no knowledge about the horizontal distribution of neutral pressure controlling the electron-neutral collision frequency.

Defining the magneto-ionic state vector $s \in (X,Y_l,Y_t,Z)$, we have the transformations

$$n^2_{p_i} = n^2_{s_k} s_{k,p_i} \tag{A5}$$

$$n^2_{p_i,p_j} = n^2_{s_k,s_l} s_{k,p_i} s_{l,p_j} + n^2_{s_k} s_{k,p_i,p_j} \tag{A6}$$

In this way, the gradient and Hessian of the square of the index of refraction are related to the gradient and Hessian of the magneto-ionic parameters. Calculating the various terms that enter into Equations A5 and A6 is regrettably tedious. Computer algebra can simplify the calculations considerably here as well.

The plasma number density profile $n_e(r) = n_e(R_e + h)$ is parameterized in the vertical in terms of either Chapman functions or semi-Epstein functions as described above. In either case, five parameters control the shape of the profile. Each of the five parameters is expanded in a bicubic B-spline basis spanning the range of colatitudes and longitudes included in the model space, that is, $d1 \cdots d5 = d1(\theta,\phi) \cdots d5(\theta,\phi)$. The gradient and Hessian of the magneto-ionic parameter X in terms of the ray parameters p then become:

$$X_r / a = n_{e,h} \tag{A7}$$

$$X_{r,r} / a = n_{e,h,h} \tag{A8}$$

$$X_{r,\theta} / a = n_{e,h,d_k} d_{k,\theta} \quad X_{r,\phi} / a = n_{e,h,d_k} d_{k,\phi} \tag{A9}$$

$$X_\theta / a = n_{e,d_k} d_{k,\theta} \quad X_\phi / a = n_{e,d_k} d_{k,\phi} \tag{A10}$$

$$X_{\theta,\theta} / a = n_{e,d_k,d_l} d_{k,\theta} d_{l,\theta} + n_{e,d_k} d_{k,\theta,\theta} \tag{A11}$$

$$X_{\theta,\phi} / a = n_{e,d_k,d_l} d_{k,\theta} d_{l,\phi} + n_{e,d_k} d_{k,\theta,\phi} \tag{A12}$$

$$X_{\phi,\phi} / a = n_{e,d_k,d_l} d_{k,\phi} d_{l,\phi} + n_{e,d_k} d_{k,\phi,\phi} \tag{A13}$$

where the constant $a \equiv e^2 / \epsilon m_e \omega$. Here again, the gradients and Hessians of n_e are most easily computed with the aid of computer algebra. The $d_k(\theta,\phi)$ parameters are polynomial functions, and the corresponding gradients and Hessians are themselves straightforward to calculate.

The Y_t and Y_l gradients and Hessians are calculated in part with the help of the IGRF-20 magnetic field model. The terms that involve purely spatial derivatives are calculated entirely using finite differences with a 19-point stencil. The terms that involve purely wavenumber derivatives are calculated strictly analytically. Cross-derivative Hessian terms involving both spatial and wavenumber gradients are computed with a hybrid approach. Wavenumber gradients are computed analytically, and spatial gradients are computed using finite differences. The spatial gradients of the magnetic field used to calculate Y are computed using the same stencil referenced above.

Insofar as the calculation of the gradient and Hessian of Y_t, the purely spatial components are computed with finite differences as with Y_l. For the remaining terms, it is expedient to begin with the results for Y_l and apply the following transformations:

$$Y_{t,p_i} = \frac{1}{Y_t}\left(YY_{p_i} - Y_l Y_{l,p_i}\right)$$

$$Y_{t,p_i,p_j} = \frac{1}{Y_t}\left(Y_{p_i}Y_{p_j} + YY_{p_ip_j} - Y_{l,p_i}Y_{l,p_j} - Y_l Y_{l,p_i,p_j} - Y_{t,p_i}Y_{t,p_j}\right)$$

where, we note that the wavenumber derivatives of Y and therefore the cross-derivative terms $Y_{p_i}Y_{p_j}$ involving wavenumber derivatives are zero.

Finally, the Z parameter depends only on the range r, and its first and second derivatives with respect to r are trivial for the case of the bi-exponential effective electron-neutral collision frequency profile considered here.

Data Availability Statement

Data used for this publication are available through the Madrigal database at Jicamarca (see http://jro.igp.gob.pe/madrigal/index.html.)

Acknowledgments

This work was supported by award FA9550-12-1-0462 from the Air Force Office of Scientific Research and by DARPA under Department of the Interior D19AC00009 to the Georgia Institute of Technology with subaward to Cornell University. The Jicamarca Radio Observatory is a facility of the Instituto Geofisíco del Perú operated with support from NSF award AGS-1732209 through Cornell. The help of the staff is much appreciated.

References

Abdu, M. A., Kherani, E. A., Batista, I. S., de Paula, E. R., Fritts, D. C., & Sobral, J. H. A. (2009). An evaluation of the ESF/bubble irregularity growth conditions under gravity wave influences based on observational data from the SpreadFEx campaign. *Annales Geophysicae*, *27*, 2607–2622. https://doi.org/10.5194/angeo-27-2607-2009

Aveiro, H. C., Hysell, D. L., Park, J., & Luhr, H. (2011). Equatorial spread F-related currents: Three-dimensional simulations and observations. *Geophysical Research Letters*, *38*, L21103. https://doi.org/10.1029/2011gl049586

Bartholomew-Biggs, M., Brown, S., Christianson, B., & Dixon, L. (2000). Automatic differentiation of algorithms. *Journal of Computational and Applied Mathematics*, *124*(1–2), 171–190. https://doi.org/10.1016/S0377-0427(00)00422-2

Bianchi, C., Baskaradas, J. A., Pezzopane, M., Pietrella, M., Sciacca, U., & Zuccheretti, E. (2013). Fading in the HF ionospheric channel and the role of irregularities. *Advances in Space Research*, *52*, 403–411. https://doi.org/10.1016/j.asr.2013.03.035

Booker, H. G., & Wells, H. W. (1938). Scattering of radio waves by the F region. *Terrestrial Magnetism*, *43*, 249. https://doi.org/10.1029/te043i003p00249

Bourne, H. (2016). *Algorithm for accurate ionospheric total electron content and receiver bias estimation using GPS measurements (MS Thesis)*. Colorado State University.

Bourne, H., Morton, Y., van Graas, F., Sulzer, M., & Milla, M. (2016). Spacial gradient based TEC estimation algorithm with code noise multipath correction evaluation using simultaneous incoherent scatter radar measurements. Proceedings of the 2016 International Technical Meeting of the Institute of Navigation (pp. 140–150). https://doi.org/10.33012/2016.13398

Budden, K. G. (1985). *The propagation of radio waves*. Cambridge Univ. Press.

Budden, K. G. (1991). Ray tracing and the effect of ray divergence and convergence on signal amplitude. *Proceedings of the Royal Society of London A*, *432*, 233–246. https://doi.org/10.1098/rspa.1991.0015

Cacuci, D. G., Weber, C. F., Oblow, E. M., & Marable, H. (1980). Sensitivity theory for general systems of nonlinear equations. *Nuclear Science & Engineering*, *75*, 88–110. https://doi.org/10.13182/nse75-88

Cao, Y., Li, S., Petzold, L., & Serban, R. (2003). Adjoint sensitivity analysis for differential algebraic equations. *Journal of Scientific Computing*, *23*(3), 1076–1089. https://doi.org/10.1137/s1064827501380630

Chapagain, N. P., Fejer, B. G., & Chau, J. L. (2009). Climatology of postsunset equatorial spread F over Jicamarca. *Journal of Geophysical Research*, *A07307*. https://doi.org/10.1029/2008JA013911

Coleman, C. J. (2011). Point-to-point ionospheric ray tracing by a direct variational method. *Radio Science*, *46*, RS5016. https://doi.org/10.1029/2011RS004748

Cummer, S. A., Inan, U. S., & Bell, T. F. (1998). Ionospheric D region remote sensing using VLF radio atmospherics. *Radio Science*, *33*(6), 1781–1792. https://doi.org/10.1029/98rs02381

Davies, K. (1965). *Ionospheric radio propagation (No. 80)*. National Bureau of Standards Monograph, U.S. Govt. Printing Office.

De-Boor, C. (1978). *A practical guide to splines*. Springer Verlag.

Farley, D. T., Balsley, B. B., Woodman, R. F., & McClure, J. P. (1970). Equatorial spread F: Implications of VHF radar observations. *Journal of Geophysical Research*, *75*, 7199–7216. https://doi.org/10.1029/ja075i034p07199

Hairer, E., & Wanner, G. (1990). *Solving ordinary differential equations II. Stiff and differential-algebraic problems*. Springer-Verlag.

Huang, C. S., Kelley, M. C., & Hysell, D. L. (1994). Nonlinear Rayleigh-Taylor instabilities, atmospheric gravity waves, and equatorial spread F. *Journal of Geophysical Research*, *98*(15), 631.

Hwang, J., Dougherty, E., Rabitz, S., & Rabitz, H. (1978). The Green's function method of sensitivity analysis in chemical kinetics. *The Journal of Chemical Physics*, *69*, 5180–5191. https://doi.org/10.1063/1.436465

Hysell, D. L., Baumgarten, Y., Milla, M. A., Valdez, A., & Kuyeng, K. (2018). Ionospheric specification and space weather forecasting with an HF beacon network in the Peruvian sector. *Journal of Geophysical Research*, *123*, 6851–6864. https://doi.org/10.1029/2018JA025648

Hysell, D. L., & Burcham, J. (1998). JULIA radar studies of equatorial spread F. *Journal of Geophysical Research*, *103*(29), 155. https://doi.org/10.1029/98ja02655

Hysell, D. L., & Chau, J. L. (2001). Inferring E region electron density profiles at Jicamarca from Faraday rotation of coherent scatter. *Journal of Geophysical Research*, *106*, 30371–30380. https://doi.org/10.1029/2000JA001101

Hysell, D. L., Jafari, R., Milla, M. A., & Meriwether, J. W. (2014). Data-driven numerical simulations of equatorial spread F in the Peruvian sector. *Journal of Geophysical Research*, *119*, 3815–3827. https://doi.org/10.1002/2014JA019889

Hysell, D. L., Milla, M. A., Condori, L., & Vierinen, J. (2015). Data-driven numerical simulations of equatorial spread F in the Peruvian sector 3: Solstice. *Journal of Geophysical Research*, *120*, 10809–10822. https://doi.org/10.1002/2015JA021877

Hysell, D. L., Milla, M. A., & Vierinen, J. (2016). A multistatic HF beacon network for ionospheric specification in the Peruvian sector. *Radio Science*, *51*, 392–401. https://doi.org/10.1002/2016RS005951

Hysell, D. L., Rao, S., Groves, K. M., & Larsen, M. F. (2020). Radar investigation of postsunset equatorial ionospheric stability over Kwajalein during project WINDY. *Journal of Geophysical Research*, *125*. https://doi.org/10.1029/2020ja027997

Jones, R. M., & Stephenson, J. J. (1975). *A versatile three-dimensional ray tracing computer program for radio waves in the ionosphere (Tech. Rep. No. 75–76)*. U. S. Department of Commerce.

Kelley, M. C., Larsen, M. F., La Hoz, C., & McClure, J. P. (1981). Gravity wave interaction of equatorial spread F: A case study. *Journal of Geophysical Research*, *86*, 9087. https://doi.org/10.1029/ja086ia11p09087

Keskinen, M. J., Ossakow, S. L., & Chaturvedi, P. K. (1980). Preliminary report of numerical simulations of intermediate wavelength collisional Rayleigh-Taylor instability in equatorial spread F. *Journal of Geophysical Research*, *85*, 1775. https://doi.org/10.1029/ja085ia04p01775

Keskinen, M. J., & Vadas, S. L. (2009). Three-dimensional nonlinear evolution of equatorial ionospheric bubbles with gravity wave seeding and tidal wind effects. *Geophysical Research Letters*, *36*, L12102. https://doi.org/10.1029/2009GL037892

Krall, J., Huba, J. D., & Fritts, D. C. (2013). On the seeding of equatorial spread F by gravity waves. *Geophysical Research Letters*, *40*(4), 661–664. https://doi.org/10.1002/GRL.50144

Krall, J., Huba, J. D., Joyce, G., & Zalesak, T. (2009). Three-dimensional simulation of equatorial spread-F with meridional wind effects. *Annales Geophysicae*, *27*, 1821–1830. https://doi.org/10.5194/angeo-27-1821-2009

Kudeki, E., Farley, D. T., & Fejer, B. G. (1982). Long wavelength irregularities in the equatorial electrojet. *Geophysical Research Letters*, *9*, 684–687. https://doi.org/10.1029/gl009i006p00684

Landau, L. D., & Lifshitz, E. M. (1976). *Mechanics* (3rd ed.). Elsevier.

McCormick, J. C. (2019). *D region tomography: A technique for ionospheric imaging using lightning-generated sferics and inverse modeling (Unpublished doctoral dissertation)*. Georgia Technical Institute.

Nava, B., Coïsson, P., & Radicella, S. M. (2008). A new version of the NeQuick ionosphere electron density model. *Journal of Atmospheric and Solar-Terrestrial Physics*, *70*, 1856–1862. https://doi.org/10.1016/j.jastp.2008.01.015

Nickisch, L. J. (1988). Focusing in the stationary phase approximation. *Radio Science*, *23*(2), 171–182. https://doi.org/10.1029/rs023i002p00171

Nodet, M., & Vidard, A. (2016). Variational methods. In G. Roger, H. David, O. Houman (Eds.), *Handbook of uncertainty quantification* (pp. 1–20). Springer International Publishing. https://doi.org/10.1007/978-3-319-11259-6_32-1

Ossakow, S. L. (1981). Spread F theories—A review. *Journal of Atmospheric and Terrestrial Physics*, *43*, 437–452. https://doi.org/10.1016/0021-9169(81)90107-0

Otsuka, Y. (2018). Review of the generation mechanisms of post-midnight irregularities in the equatorial and low-latitude ionosphere. *Progress in Earth and Planetary Science*, *5*(57), 1–13. https://doi.org/10.1186/s40645-018-0212-7

Psiaki, M. (2019). Ionosphere ray tracing of radio-frequency signals and solution sensitivities to model parameters. *Radio Science*, *54*, 738–757. https://doi.org/10.1029/2019RS006792

Psiaki, M. L., Bust, G. S., & Mitchell, C. N. (2015). Nonlinear estimation to assimilate GPS TEC data into a regional ionosphere model. Proceedings of the 28th International Technical Meeting of the Satellite Division of the Institute of Navigation (ION GNSS+ 2015) (pp. 3497–3510).

Rao, S. V. B., Rao, T. R., Reddy, V. G., Lakshmi, D. R., Veenadhari, B., Dabas, R. S., et al. (2002). HF radio signal fading and atmospheric radio noise measurements at low latitudes. *Radio Science*, *37*(5), 1–7. https://doi.org/10.1029/2001RS002495

Reyes, P. M., Kudeki, E., Lehmacher, G. A., Chau, J. L., & Milla, M. A. (2020). VIPIR and 50 MHz radar studies of gravity wave signatures in 150-km echoes observed at Jicamarca. *Journal of Geophysical Research*, *125*, e2019JA027535. https://doi.org/10.1029/2019JA027535

Röttger, J. (1981). Equatorial spread F by electric fields and atmospheric gravity waves generated by thunderstorms. *Journal of Atmospheric and Terrestrial Physics*, *43*, 453–462. https://doi.org/10.1016/0021-9169(81)90108-2

Salaman, R. K. (1962). *Historical survey of fading at medium and high frequencies (Tech. Rep. No. 133)*. National Bureau of Standards.

Sambridge, M. S., & Kennett, B. L. N. (1990). Boundary value ray tracing in a heterogeneous medium: A simple and versatile algorithm. *Geophysical Journal International*, *101*, 157–168. https://doi.org/10.1111/j.1365-246x.1990.tb00765.x

Schunk, R., & Nagy, A. (2009). *Ionospheres: Physics, plasma physics, and chemistry* (2nd ed.). Cambridge University Press.

Sen, H. K., & Wyller, A. A. (1960). On the generalization of the Appleton-Hartree magnetoionic formulas. *Journal of Geophysical Research*, *65*, 3931–3950. https://doi.org/10.1029/jz065i012p03931

Settimi, A., Pietrella, M., Pezzopane, M., & Bianchi, C. (2015). The IONORT-ISP-WC system: Inclusion of an electron collision frequency model for the D-layer. *Advances in Space Research*, *55*, 2114–2123. https://doi.org/10.1016/j.asr.2014.07.040

Singh, S., Johnson, F. S., & Power, R. A. (1997). Gravity wave seeding of equatorial plasma bubbles. *Journal of Geophysical Research*, *102*, 7399–7410. https://doi.org/10.1029/96ja03998

Taori, A., Patra, A. K., & Joshi, L. M. (2011). Gravity wave seeding of equatorial plasma bubbles: An investigation with simultaneous F-region, E-region, and middle atmospheric measurements. *Journal of Geophysical Research*, *116*. https://doi.org/10.1029/2010ja016229

Tromp, J., Tape, C., & Liu, Q. (2005). Seismic tomography, adjoint methods, time reversal and banana-doughnut kernels. *Geophysical Journal International*, *160*, 195–216.

Tsunoda, R. T. (2010). On seeding equatorial spread F: Circular gravity waves. *Geophysical Research Letters*, *37*, L10104. https://doi.org/10.1029/2010GL043422

Tsunoda, R. T., Barons, M. J., Owen, J., & Towle, D. M. (1979). Altair: An incoherent scatter radar for equatorial spread F studies. *Radio Science*, *14*, 1111–1119. https://doi.org/10.1029/rs014i006p01111

Tsunoda, R. T., Bubenik, D. M., Thampi, S. V., & Yamamoto, M. (2010). On large-scale wave structure and equatorial spread F without a post-sunset rise of the F layer. *Geophysical Research Letters*, *37*, L07105. https://doi.org/10.1029/2009GL042357

Västberg, A., & Lundborg, B. (1996). Signal intensity in the geometric optics approximation for the magnetized ionosphere. *Radio Science*, *31*(6), 1579–1588. https://doi.org/10.1029/96rs02630

Woodman, R. F., Chau, J. L., & Ilma, R. R. (2006). Comparison of ionosonde and incoherent scatter drift measurements at the magnetic equator. *Geophysical Research Letters*, *33*, L01103. https://doi.org/10.1029/2005GL023692

Woodman, R. F., & La Hoz, C. (1976). Radar observations of F region equatorial irregularities. *Journal of Geophysical Research*, *81*, 5447–5466. https://doi.org/10.1029/ja081i031p05447

Yokoyama, T., Shinagawa, H., & Jin, H. (2014). Nonlinear growth, bifurcation and pinching of equatorial plasma bubble simulated by three-dimensional high-resolution bubble model. *Journal of Geophysical Research: Space Physics*, *119*(10), 10474–10482. https://doi.org/10.1002/2014ja020708

Zalesak, S. T., Drake, J. F., & Huba, J. D. (1990). Three-dimensional simulation study of ionospheric plasma clouds. *Geophysical Research Letters*, *17*(10), 1597–1600. https://doi.org/10.1029/gl017i010p01597

Zalesak, S. T., Ossakow, S. L., & Chaturvedi, P. K. (1982). Nonlinear equatorial spread F—The effect of neutral winds and background Pedersen conductivity. *Journal of Geophysical Research*, *87*, 151–166. https://doi.org/10.1029/ja087ia01p00151

Zargham, S., & Seyler, C. E. (1987). Collisional interchange instability, 1, Numerical simulations of intermediate-scale irregularities. *Journal of Geophysical Research*, *92*, 10073. https://doi.org/10.1029/ja092ia09p10073

Zargham, S., & Seyler, C. E. (1989). Collisional and inertial dynamics of the ionospheric interchange instability. *Journal of Geophysical Research*, *94*, 9009. https://doi.org/10.1029/ja094ia07p09009

Zawdie, K. A., Drob, D. P., Siskind, D. E., & Coker, C. (2017). Calculating the absorption of HF radio waves in the ionosphere. *Radio Science*, *52*, 767–783. https://doi.org/10.1002/2017RS006256